2025 47th Annual International Conference of the IEEE Engineering in Medicine and Biology Society (EMBC) | 979-8-3315-8618-8/25/$31.00 ©2025 Authors | DOI: 10.1109/EMBC58623.2025.11251769

Arbitrary Waveform Multi-Lead Temporal Interference Stimulation

Lukas Geisshuesler[1], *Student Member, IEEE,* Elisa Maria Kaufmann[1], Julian Piller[1], Andreas Haeberlin[2]
and Thomas Niederhauser[1], *Member, IEEE*

Abstract— **Temporal interference stimulation (TIS) is used as a spatially selective tool for electrical deep brain stimulation in research applications. Despite its advantages over conventional stimulation methods, most of the current TIS systems are constrained by their reliance on only two leads and purely sinusoidal signals. Multi-lead and arbitrary waveform TIS may provide enhanced control over the stimulation location in a 2D plane or 3D space and the stimulation efficiency, respectively. This paper presents a novel therapeutic system for multi-lead arbitrary waveform TIS. The system uses a Direct Digital Synthesis (DDS) integrated circuit (IC) as a signal generator and a voltage-controlled constant current source, based on a Howland current pump, as an output stage to generate arbitrary signals. A frequency range from 100Hz to 1.5MHz (with a current gain of -3dB point at 1.5MHz into a 10kΩ load) and a current range from 0 to 80mA were achieved. This performance enables, for example, the generation of rectangular interference pulses with a duration of 10μs using five harmonics. This is a substantial increase over commonly used signal sources in TIS research, which typically operate at maximum frequencies between 20kHz and 400kHz. The system was evaluated in an *in vitro* experiment using a saline solution to characterize the interference patterns generated by three channels. The results obtained were in line with simulations and confirmed the system's capability to produce consistent and spatially precise temporal interference (TI) patterns in a 2D plane. Combined with the arbitrary waveform capacity, the system has high potential for advanced electrical therapies with TIS beyond deep brain stimulation, such as nerve, muscle, or cardiac stimulation.**

I. INTRODUCTION

TIS has gained attention as a promising neuromodulation technique due to its ability to target deep neural structures without directly stimulating superficial tissues. The basic principle of TIS involves applying two or more electric fields with high-frequency carrier signals, which exhibit a small frequency offset, creating a specific interference pattern. The tissue responds to the envelope of this interference pattern that oscillates at the frequency of the offset between the carriers, rather than at the carrier frequencies themselves [1][2]. The maximum interference location—at which the two carrier signals interfere totally, leading to the highest relative envelope amplitude—is determined by the current distribution between the electrode pairs and the geometrical orientation of the electrodes. The ability to control the location of the interference, and therefore the location of the stimulation, offers the potential for highly selective stimulation, even in cases where the electrodes cannot be optimally positioned close to the target structures [1][3].

Recent studies indicate that TIS can be applied to peripheral nerves to innervate skeletal muscles [4]. Moreover, waveforms other than sinusoidal signals can be used, such as pulse-width modulation (PWM)-TIS utilizing square waves as carrier signals [5]. This is particularly relevant since the shape of the pulse wave may influence the excitation level of the targeted structures, possibly further reducing unwanted co-stimulations of adjacent tissue [6]. Using Fourier series-based carrier signals may even provide a higher degree of flexibility to adjust the interference pattern to specific targeted structures, such as peripheral nerves, motor nerves to innervate muscles, and cardiac tissue. One application of the arbitrary waveform TIS could be the transesophageal stimulation of the phrenic nerves in mechanically ventilated patients to reduce ventilator-induced diaphragmatic dysfunction while reducing unwanted co-stimulation of e.g., stimulation of the vagus nerve [7]. To this end, a platform for multi-lead electrical arbitrary waveform stimulation was developed. The unique TIS platform supports a wide range of current and frequency settings with a large output voltage compliance, enabling its application to various target structures. Furthermore, it allows the application of techniques used in conventional stimulation, such as ramping up the amplitude during stimulation. More than two leads, i.e. multiple lead TIS, allows the maximum interference location to be controlled not only along a line between two electrode pairs, but also across a 2D plane or even in a 3D space. The design and development of the system were guided by relevant standards, such as IEC 60601-1 or IEC 60601-2-10, to achieve the required safety and performance of the nerve and muscle stimulator system, guaranteeing safe and reliable operation.

II. METHODS

A. FOURIER SERIES TIS

We propose the use of a Fourier series for the construction of the TIS carrier signals, called hereafter FS-TIS, which allows modeling of the desired interference waveform without restrictions. For the present case, the aim was to model the interference pattern as a square wave by combining the fundamental frequency and its first $n-1$ odd harmonics. The resulting interference combines the characteristics of PWM-TIS (i.e., the modulation of the pulse width due to interference) and TIS based on sinusoidal carrier frequencies (i.e., the modulation of the amplitude due to interference) as

---

*This work was supported by the Swiss National Science Foundation SNSF with grant number CRSK-3_228913 / 1

[1] Institute for Human Centered Engineering HuCE, Bern University of Applied Sciences, Biel, Switzerland

[2] Department of Cardiology, Bern University Hospital, University of Bern, Bern, Switzerland

shown in Figure 1. Although the behavior of FS-TIS is similar to that of PWM-TIS, indicated as near constant amplitude when constructive interference is present, the amplitude is reduced when the carrier signals interfere destructively, as it is typical for regular sinusoidal waveforms. The combination of constructive and destructive interference leads to the modulation of both, the pulse width and the pulse envelope, leading to the hypothesis that FS-TIS may result in more efficient stimulation of the target structure.

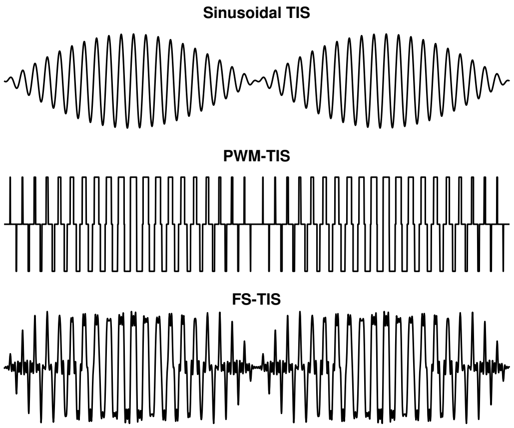

Fig. 1. Comparison of sinusoidal TIS, PWM-TIS, and FS-TIS with total interference (i.e., carrier signal amplitudes are equal at the location of interference). FS-TIS uses a 5th-order square wave Fourier Series as carrier signals.

B. *AMPLIFIER SYSTEM DESIGN*

1) Main Board: The central component of the main board that is used to control the stimulator is a Xilinx Zynq-7000 system-on-chip (SoC). One of its two CPU cores runs a C++ program that facilitates communication with a PC via an Ethernet interface using the JSON-RPC protocol. This program configures the stimulator signal generator based on the desired stimulation settings.

The FPGA section of the SoC is used to read and process measurements from three 16-bit, 25MSs^{-1} dual-channel ADCs integrated on the main board. Measurements indicate that the effective number of bits (ENOB) for the setup is 12. These ADCs monitor the stimulation current applied and the resulting voltage for each of the three output stages. The acquired data can, for example, be used to evaluate the signals during stimulation or to verify the proper connection of the electrodes prior to stimulation. Figure 2 shows an overview of the main board, waveform generators, and modular output stages.

2) Waveform Generation: To generate various TIS waveforms, the AD9102 direct digital synthesis (DDS) integrated circuit (IC) from Analog Devices (Massachusetts, USA) was employed. In addition to its basic DDS functionality, which supports the generation of sinusoidal, sawtooth, and triangular signals, this IC features a 4096×14-bit deep SRAM that enables storage of arbitrary waveforms. Each DDS includes a logic trigger input to switch the outputs on or off and to synchronize multiple ICs. These features significantly reduce the number of required connections and the overall system complexity compared to an FPGA-based implementation with separate DACs. Additionally, this IC simplifies software timing requirements, as it is pre-programmed before stimulation and subsequently can be triggered synchronously via a hardware trigger. To maximize the flexibility of the output signal using the SRAM, a programmable oscillator enables the internal SRAM to be activated over a wide clock range f_{clk} from 100kHz to 180MHz with a frequency resolution of 0.26ppm.

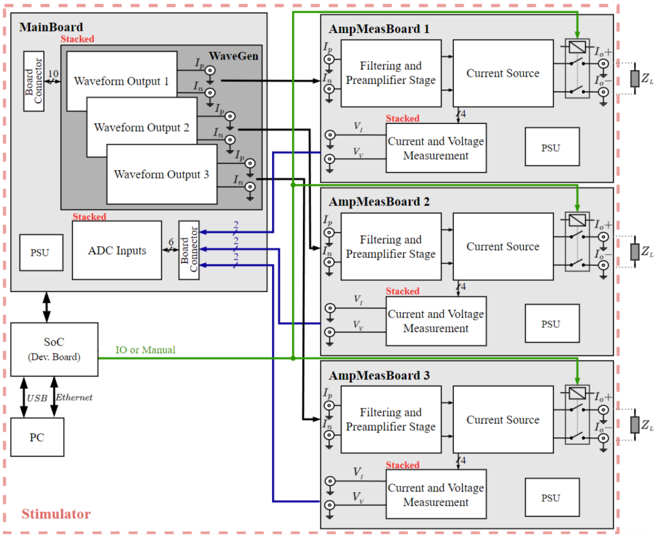

Fig. 2. Overview of the main components of the novel arbitrary waveform TIS platform.

3) Output Stage: To achieve the desired modularity of the system, each output stage is designed to operate independently. The output stage features a dedicated low-voltage power supply unit that converts ±15V and ±5V from an externally applied 12V input. A filtering and pre-amplification stage processes the differential current output signals from the custom waveform generator. First, the differential current signal is converted into a differential voltage signal. This signal is then passed through a reconstruction filter to eliminate quantization steps from the internal DAC of the DDS IC. After filtering, the voltage signals are pre-amplified and routed to the current source input. The stimulation current applied for TIS is generated incorporating an improved Howland current pump in a bipolar bridge configuration using an additional inverting unity gain amplifier as shown in Figure 3. This source and sink configuration not only increases the output voltage compliance and is expected to reduce the amount of crosstalk between the TIS channels, too, leading to an improved stimulation focality [1]. To meet the target performance requirements, a PA198 high-end power operational amplifier from Apex Microtechnology (Arizona, USA) was selected. This operational amplifier can be supplied with up to ±225V, has a continuous output current of up to 200mA, and a slew rate of $2\text{kV}\mu\text{s}^{-1}$. Despite its large voltage compliance, the amplifier still provides a large power bandwidth and low noise operation. To enhance precision and performance for a wide range of stimulation currents, two current ranges, one ranging from 0 to 80mA and the other one from 0 to 8mA, are achieved by two switchable current feedback paths for the Howland current pump. Although there is no galvanic isolation between the output stages or the signal waveform generators, the entire setup is powered by an isolated medical-grade power supply and incorporates an Ethernet isolator to prevent unwanted leakage currents.

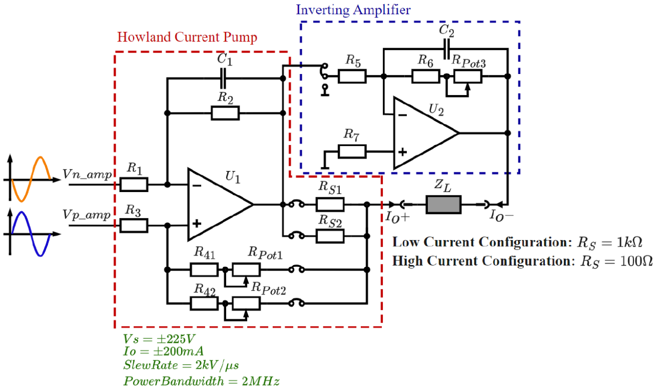

Fig. 3. Schematic of the Howland current pump-based output stage with two switchable output current ranges.

C. AMPLIFIER PERFORMANCE AND IN VITRO MEASUREMENTS

The functionality and performance of the waveform generator, measurement board, and output stage were individually assessed on the bench. The proof of arbitrary waveform multi-lead TIS is given by a dedicated *in vitro* experiment, in which the three stimulation outputs generated TI patterns measured in a saltwater bath with fixed, homogeneous conductivity. This controlled environment enabled a simplified yet precise evaluation of the interference behavior among the three outputs with respect to envelope modulation amplitude at a specific location. Figure 4 depicts the triangular arrangement of the three electrode pairs used during the measurements. Each pair was driven by a sinusoidal or Fourier series constructed rectangular current with base carrier frequencies $f_{\text{red}} = 100\text{kHz}$ and $f_{\text{blue}} = f_{\text{green}} = 101\text{kHz}$, respectively. Results are shown for load impedances between 1kΩ and 10kΩ, mimicking general skin and tissue impedance for the desired frequency range and typical values for noninvasive transcranial alternating current stimulation and cardiac stimulation [8][9][10].

To minimize the time and resources required for extensive measurements, a computational simulation framework was developed following the method proposed by Mirzakhalili et al. [2]. The potential field generated by a monopolar current source is calculated using Equation 1, where $I(t)$ represents the time-varying current of the source (e.g. $I(t) = I_0 \cdot \sin(2\pi f t + \phi)$) and the spatial coordinates of the electrode are denoted by x_s, y_s, z_s. The conductivity tensor components $\sigma_{xx}, \sigma_{yy}, \sigma_{zz}$ define the anisotropic conductivity of the medium along the respective Cartesian axes. Under these conditions, the total potential field at any point in time is obtained by superimposing the contributions of all individual current sources, as described in Equation 2, with each source characterized by its amplitude and frequency. The size of the simulation volume, as well as the spatial and temporal resolution at which the potential $V(x,y,z,t)$ is evaluated, can be tailored to a specific application. This simulation tool enables rapid optimization of stimulation parameters to control the location of maximum interference at a desired target location for a given electrode setup. To validate the accuracy of the simulated interference patterns, they were compared to the *in vitro* measurements using the same lead orientation and conductivity. While an analytical determination of the envelope based on the Hilbert transform can be used for sinusoidal TIS; however, this method is not well suited for the high frequency peaks present in FS-TIS. Therefore, a custom numerical approach was used to compute the envelope by detecting the peaks and fitting a third-order polynomial spline between them.

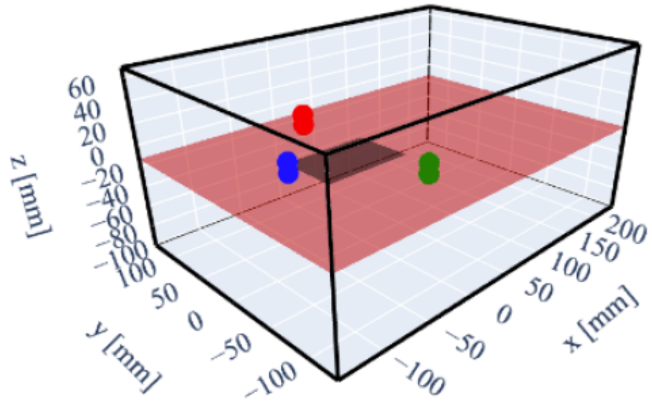

Fig. 4. *In vitro* measurement setup for interference patterns generated by three sinusoidal carrier sources located at $S_{\text{red}}(x = 0\text{mm}, y = -80\text{mm})$, $S_{\text{green}}(x = 0\text{mm}, y = 80\text{mm})$, and $S_{\text{blue}}(x = -80\text{mm}, y = 0\text{mm})$. The carrier frequencies were $f_{\text{red}} = 100\text{kHz}$ and $f_{\text{blue}} = f_{\text{green}} = 101\text{kHz}$. The homogeneous volume conductivity was set to $\sigma_{xx} = \sigma_{yy} = \sigma_{zz} = 0.14$. The red plane indicates the height at which the envelope modulation amplitude was plotted, while the gray square outlines the displayed area.

$$V(x,y,z,t) = \frac{I(t)}{4\pi\sqrt{\sigma_{xx}\sigma_{yy}\sigma_{zz}}} \cdot \frac{1}{\frac{(x-x_s)^2}{\sigma xx} + \frac{(y-y_s)^2}{\sigma yy} + \frac{(z-z_s)^2}{\sigma zz}} \tag{1}$$

$$V_{tot}(x,y,z,t) = \sum_{n=1}^{N_s} V_n(x,y,z,t) \tag{2}$$

D. STEERABILITY OF MULTI-LEAD TIS

To demonstrate the advantages of multi-lead TIS that allow control over the location of maximum interference within a plane or a volumetric region, simulations were conducted to evaluate the steerability of the maximum relative envelope modulation amplitude of the electric field. In these simulations, currents of varying amplitudes were applied to three TIS electrode pairs, and the location of the highest relative envelope modulation amplitude was identified and marked. The same simulation environment as for measurement validation was used.

III. RESULTS

A. *AMPLIFIER PERFORMANCE*

Figure 5 illustrates the output behavior when a sinusoidal current of 7.2mA is applied to loads of 1kΩ and 10kΩ across a frequency range from 100Hz to 3MHz. For the 1kΩ load, both current ranges—8mA and 80mA—are shown. The 80mA for a 10kΩ load is omitted due to the output saturation caused by reaching the maximum voltage compliance of the output stage.

For a load of $R_L = 1\text{k}\Omega$ with the current range set to 0 to 80mA (i.e. small DDS gain), the current amplitude remains stable up to 20kHz and is still above the -3dB point at 5mA for frequencies of up to 100kHz. Switching the current range to between 0 and 8mA (i.e., large DDS gain) allows the system to drive the same desired current up to 1.5MHz before crossing the -3dB point. Increasing the load to $R_L = 10\text{k}\Omega$ while maintaining the current range leads to a very similar frequency performance to that of driving the current into a load of 1kΩ and the current range set to 0 to 80mA.

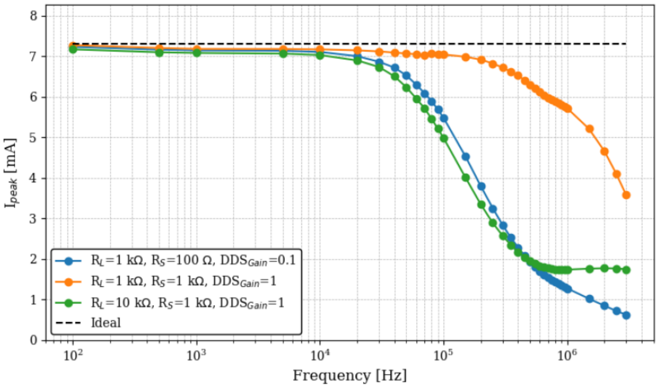

Fig. 5. Frequency dependent output performance of the TIS platform for different output loads for both output current ranges. The output current was set to 7.2mA.

B. *IN VITRO TESTS*

Figure 6 and 7 show the measured electrical fields of TI using three signal sources with carrier signals at $f_1 = f_2 = 100$kHz and $f_3 = 101$kHz based on sinusoidal and 5th order Fourier series-based square wave, respectively. The envelope beat frequency is 1kHz, the square wave has a pulse duration of 10μs. Sinusoidal TIS shows a sinusoidal envelope modulation while the FS-TIS shows a square wave-shaped envelope modulation. As expected, FS-TIS shows an additional increase in pulse width in the center of the modulation around $t = 1.5$ms and $t = 2.5$ms each, resulting in a darker shade in the plot. Increasing the order of FS-TIS would increase the flatness of the envelope and lead to steeper edges of the envelope.

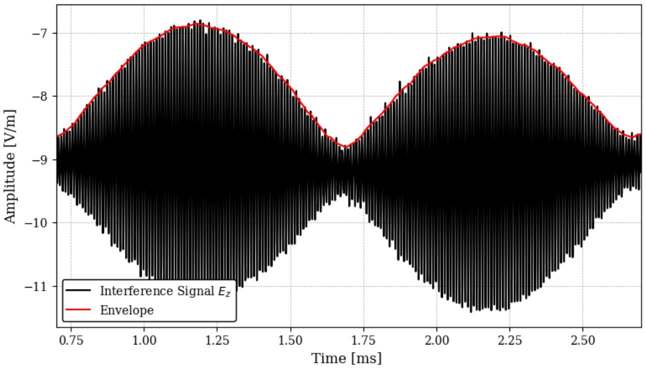

Fig. 6. *In vitro* measurement of electric field of interference using three sinusoidal carrier signals at $f_{\text{red}} = 100$kHz and $f_{\text{blue}} = f_{\text{green}} = 101$kHz with a homogeneous volume conductivity of $\sigma_{xx} = \sigma_{yy} = \sigma_{zz} = 0.14\text{Sm}^{-1}$.

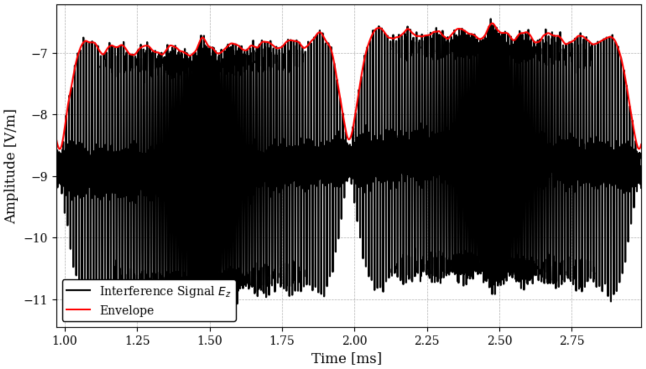

Fig. 7. *In vitro* measurement of interference using three 5th order square wave Fourier series carrier signals at first harmonic frequencies of $f_{\text{red}} = 100$kHz and $f_{\text{blue}} = f_{\text{green}} = 101$kHz with a homogeneous volume conductivity of $\sigma_{xx} = \sigma_{yy} = \sigma_{zz} = 0.14\text{Sm}^{-1}$.

The electric field was measured in an area located between the three pairs of electrodes. To visualize TI in a plane, the envelope modulation amplitude was plotted over the entire area in Figure 8. These results were compared with a simulation (Figure 9) using the same volume, electrode locations, and carrier signal parameters. With electrode frequencies of $f_{red} = 100$kHz and $f_{blue} = f_{green} = 101$kHz and a uniform current distribution between the electrodes of $I_{red} = I_{blue} = I_{green} = 10$mA, both measurements and simulation show the same behavior. A region of high envelope modulation amplitude is located between the pair of red electrodes and the pair of blue electrodes, and a maximum at $x = -40$mm and $y = 30$mm. The relative root mean square error (RRMSE) between measurement and simulation over the entire area is 17%.

C. *STEERABILITY OF MULTI-LEAD TIS*

Figure 10 illustrates locations exhibiting the maximum relative envelope modulation amplitude for a given current distribution among the three pairs of electrodes arranged

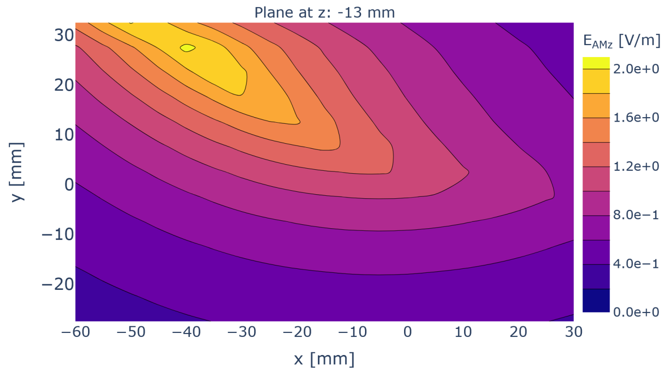

Fig. 8. *In vitro* measurement of envelope modulation amplitude of the electrical field using three sinusoidal carrier signals at $f_{red} = 100\text{kHz}$ and $f_{blue} = f_{green} = 101\text{kHz}$ and $I_{red} = I_{blue} = I_{green} = 10\text{mA}$ with a homogeneous volume conductivity of $\sigma_{xx} = \sigma_{yy} = \sigma_{zz} = 0.14\text{Sm}^{-1}$.

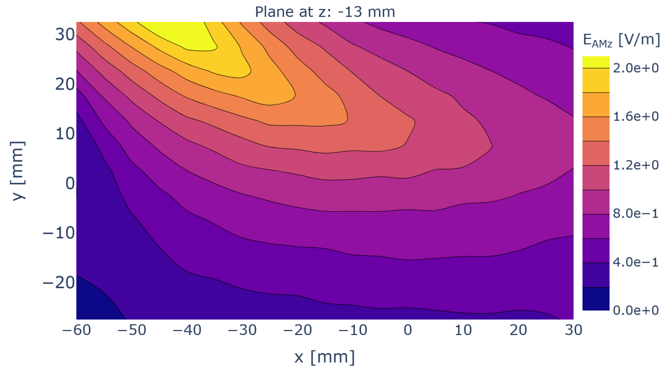

Fig. 9. Simulation of envelope modulation amplitude of the electrical field using three sinusoidal carrier signals at $f_{red} = 100\text{kHz}$ and $f_{blue} = f_{green} = 101\text{kHz}$ and $I_{red} = I_{blue} = I_{green} = 10\text{mA}$ with a homogeneous volume conductivity of $\sigma_{xx} = \sigma_{yy} = \sigma_{zz} = 0.14\text{Sm}^{-1}$.

in a triangular configuration. A carrier signal at 1kHz was applied to electrode pair 1 (red), while carrier signals at 1.1kHz were applied to electrode pairs 2 (blue) and 3 (green). Simulation of all possible current distributions between 1 and 10mA, in 1mA steps, showed that the location of maximum interference can be steered within the upper half of the triangle formed by the electrode pairs. To shift the maximum amplitude location to the lower half of the triangle, the carrier signal frequencies of electrode pairs 1 and 3 need to be swapped. Despite the overall similarities between measurement and simulation, there are still some deviations in exact location and envelope modulation amplitude.

IV. DISCUSSION

The initial characterization of the output performance confirms the system's robustness in maintaining signal integrity when combining multiple current sources and its flexibility in adjusting current, frequency, and waveform. Experimental tests demonstrated that the platform can reliably drive currents from 0mA to 80mA with a resolution of 14-bit to loads in the kΩ range, maintaining stability across a broad frequency range of 100Hz to 1.5MHz. Compared to commonly used signal sources in TIS research, which typically operate at maximum frequencies between 20kHz and 400kHz [4][5], the presented system significantly extends the usable frequency range. At higher frequencies, accurate current delivery into high-impedance loads becomes increasingly challenging due to a reduction in parallel output resistance. However, this limitation is mitigated in practical applications, as the impedance of the skin and tissue generally decreases with increasing frequency [8]. In addition, the system can be specifically calibrated for a given application to ensure consistent and accurate current delivery within the required frequency range. The integrated current and voltage measurements also enable real-time monitoring of the applied signal and the electrode impedance, allowing for adjustment of the stimulation current to improve current accuracy and, consequently, the precision of the stimulation location.

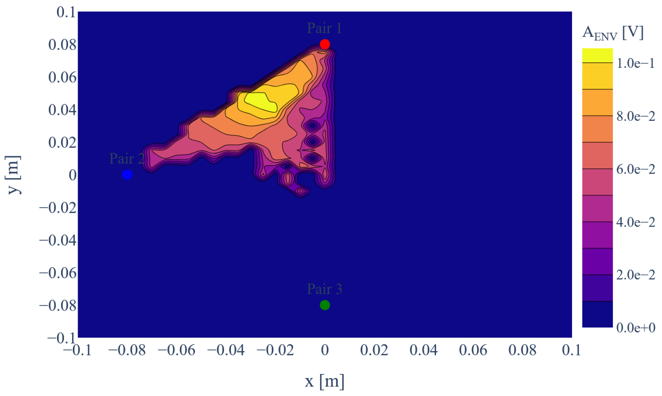

Fig. 10. Location of modulation amplitude maxima and corresponding envelope amplitude for varying current distribution with $f_{red} = 1\text{kHz}$ and $f_{blue} = f_{green} = 1.1\text{kHz}$ and a homogeneous volume conductivity of $\sigma_{xx} = \sigma_{yy} = \sigma_{zz} = 0.14\text{Sm}^{-1}$.

The system's high-frequency performance was further demonstrated in *in vitro* experiments. The system successfully generated TI using carrier signals around 100kHz, for both sinusoidal and Fourier-based interference waveforms. This represents a 20- to 100-fold increase compared to previous studies, where carrier frequencies ranged from 1kHz to 5kHz [1][3][4][5]. This expanded frequency range, combined with the ability to generate arbitrary waveforms, allows the system to create targeted interference envelope patterns that closely replicate conventional electrical stimulation waveforms, such as rectangular and biphasic pulses, while matching their pulse width. Rectangular and biphasic pulses are widely utilized in various electrical stimulation applications, with typical pulse widths ranging from several hundred microseconds to the low millisecond range [11][12][13][14].

Additionally, *in vitro* experiments confirmed that the developed platform supports multi-lead TIS, enabling more precise targeting of specific structures. The measured electric field within the area between the electrode pairs matched the simulation results in large parts, further validating the system's accuracy and reliability. A possible reason for the deviations that occurred between the measurements and the simulations could be the simplifications applied to the simulation, such as modeling the signal sources as ideal point sources. Other influences that could have led to the deviations are that the conductivity in the measurement setup may not be truly homogeneous, and possible electrode positioning errors. In contrast to the *in vitro* setup, physiological tissue typically exhibits non-homogeneous conductivity, which affects the distribution of the electric field—and consequently, the envelope amplitude modulation pattern as well as the location of maximum interference.

Simulations of the interference maximum's steerability demonstrated that employing three independent TIS sources enables precise control of the maximum interference location within a 2D plane. For the described triangular electrode arrangement, every location within the intra-electrode space could be reached. This represents a substantial improvement over systems that use only two signal sources, which restrict TIS steerability to a single line between electrode pairs [1][2]. This improved steerability could lead to a reduction in unwanted co-stimulation of physiological structures. However, further research is needed to determine whether the ability to control the interference location in a plane directly translates to improved steerability with sufficient selectivity of the stimulated region in *in vivo* applications. The continuous signals applied during TIS may interfere with EEG or ECG recordings in *in vivo* applications, depending on the targeted structure. However, this interference can be mitigated through narrowband filtering, as the frequency components of both sinusoidal TIS and FS-TIS are known *a priori*.

V. CONCLUSIONS

The presented stimulation system establishes a versatile and robust platform for advancing research in TIS. In contrast to conventional two-lead setups, the system's multi-lead capability enables control of the location of maximum interference across a 2D plane or 3D volume, rather than being restricted to a linear axis between electrodes.

Its broad current and frequency range, combined with the ability to generate arbitrary waveforms, significantly enhances its applicability beyond traditional neural stimulation. The system supports the creation of customized stimulation waveforms tailored to specific physiological targets, such as cardiac tissue and peripheral motor nerves.

A notable future application could be the stimulation of the phrenic nerve to activate the diaphragm in mechanically ventilated patients, employing physiologically optimized stimulation envelopes. This flexibility opens new opportunities for both research and therapeutic applications, enabling the optimization of stimulation protocols for various tissues and the potential improvement of therapeutic outcomes.

REFERENCES

[1] N. Grossman, D. Bono, N. Dedic, S. B. Kodandaramaiah, A. Rudenko, H. J. Suk, A. M. Cassara, E. Neufeld, N. Kuster, L. H. Tsai, A. Pascual-Leone, and E. S. Boyden, "Noninvasive deep brain stimulation via temporally interfering electric fields," *Cell*, vol. 169, pp. 1029–1041.e16, 2017. [Online]. Available: http://dx.doi.org/10.1016/j.cell.2017.05.024

[2] E. Mirzakhalili, B. Barra, M. Capogrosso, and S. F. Lempka, "Article biophysics of temporal interference stimulation," *Cell Systems*, vol. 11, pp. 1–16, 2020. [Online]. Available: https://doi.org/10.1016/j.cels.2020.10.004

[3] M. D. Sunshine, A. M. Cassarà, E. Neufeld, N. Grossman, T. H. Mareci, K. J. Otto, E. S. Boyden, and D. D. Fuller, "Restoration of breathing after opioid overdose and spinal cord injury using temporal interference stimulation," *Communications Biology*, vol. 4, pp. 1–15, 2021. [Online]. Available: http://dx.doi.org/10.1038/s42003-020-01604-x

[4] B. Botzanowski, M. J. Donahue, M. S. Ejneby, A. L. Gallina, I. Ngom, F. Missey, E. Acerbo, D. Byun, R. Carron, A. M. Cassarà, E. Neufeld, V. Jirsa, P. S. Olofsson, E. D. Głowacki, and A. Williamson, "Noninvasive stimulation of peripheral nerves using temporally-interfering electrical fields," *Advanced Healthcare Materials*, vol. 11, p. 2200075, 9 2022. [Online]. Available: https://onlinelibrary.wiley.com/doi/10.1002/adhm.202200075

[5] C. E. Luff, P. Dzialecka, E. Acerbo, A. Williamson, and N. Grossman, "Pulse-width modulated temporal interference (pwm-ti) brain stimulation," *Brain Stimulation*, vol. 17, pp. 92–103, 1 2024.

[6] M. Sahin and Y. Tie, "Non-rectangular waveforms for neural stimulation with practical electrodes," *Journal of Neural Engineering*, vol. 4, p. 227, 5 2007. [Online]. Available: https://iopscience.iop.org/article/10.1088/1741-2560/4/3/008https://iopscience.iop.org/article/10.1088/1741-2560/4/3/008/meta

[7] E. M. Kaufmann, S. Krause, L. Geisshuesler, O. Scheidegger, A. Haeberlin, and T. Niederhauser, "Feasibility of transesophageal phrenic nerve stimulation," *BioMedical Engineering Online*, vol. 22, pp. 1–14, 12 2023. [Online]. Available: https://biomedical-engineering-online.biomedcentral.com/articles/10.1186/s12938-023-01071-5

[8] J. Rosell, J. Colominas, and J. G. Webster, "Skin impedance from 1hz to 1mhz," *IEEE Transactions on Biomedical Engineering*, vol. 35, pp. 649–652, 1988.

[9] Y. Piao, R. Ma, Y. Weng, C. Fan, X. Xia, W. Zhang, G. Q. Zeng, Y. Wang, Z. Lu, J. Cui, X. Wang, L. Gao, B. Qiu, and X. Zhang, "Safety evaluation of employing temporal interference transcranial alternating current stimulation in human studies," *Brain Sciences*, vol. 12, p. 1194, 9 2022. [Online]. Available: https://pmc.ncbi.nlm.nih.gov/articles/PMC9496688/

[10] G. F. O. Tyers, R. R. Brownlee, H. C. Hughes, C. W. Shaffer, E. H. Williams, and R. L. Kao, "Myocardial stimulation impedance: The effects of electrode, physiological, and stimulus variables," *The Annals of Thoracic Surgery*, vol. 27, pp. 63–69, 1 1979.

[11] S. D. Bennie, J. S. Petrofsky, J. Nisperos, M. Tsurudome, and M. Laymon, "Toward the optimal waveform for electrical stimulation of human muscle," *European journal of applied physiology*, vol. 88, pp. 13–19, 2002. [Online]. Available: https://pubmed.ncbi.nlm.nih.gov/12436266/

[12] D. W. Benson, M. Sanford, A. Dunnigan, and D. G. Benditt, "Transesophageal atrial pacing threshold: Role of interelectrode spacing, pulse width and catheter insertion depth," *American Journal of Cardiology*, vol. 53, pp. 63–67, 1 1984. [Online]. Available: http://www.ajconline.org/article/0002914984906842/fulltexthttp://www.ajconline.org/article/0002914984906842/abstracthttps://www.ajconline.org/article/0002-9149(84)90684-2/abstract

[13] M. Johnson, "Transcutaneous electrical nerve stimulation: Mechanisms, clinical application and evidence," *Reviews in Pain*, vol. 1, p. 7, 8 2007. [Online]. Available: https://pmc.ncbi.nlm.nih.gov/articles/PMC4589923/

[14] B. M. Doucet, A. Lam, and L. Griffin, "Neuromuscular electrical stimulation for skeletal muscle function," *The Yale Journal of Biology and Medicine*, vol. 85, p. 201, 6 2012. [Online]. Available: https://pmc.ncbi.nlm.nih.gov/articles/PMC3375668/